nature communications

Article

https://doi.org/10.1038/s41467-026-72894-8

Energy-efficient field-free switching by orbital torque and spin-reorientation

Received: 24 October 2025

Accepted: 27 April 2026

Published online: 08 May 2026

Check for updates

Bilal Jamshed[1,3], Subhakanta Das[1,3], Pinkesh Kumar Mishra[1], Wai Lum William Mah[1], Mathias Kläui[2] & S. N. Piramanayagam[1] ✉

Spin-orbit torque has emerged as a leading strategy for low-power magnetisation switching in modern spintronics. To date, most efforts have focused on boosting spin currents via the spin Hall effect, exploiting only the electron's spin while largely ignoring its orbital angular momentum. Meanwhile, deterministic switching of perpendicular magnetic anisotropy layers typically requires an external in-plane field to break inversion symmetry, adding power overhead and hindering large-scale deployment. Here, we demonstrate energy-efficient field-free magnetisation switching enabled by spin reorientation in a synthetic antiferromagnetic structure and enhanced by orbital torque. By tuning the exchange coupling field and magnetic anisotropy of the synthetic antiferromagnetic samples, we achieved a magnetisation switching of 96% utilising both spin and orbital torque. Furthermore, increasing the orbital Hall layer thickness by 15 nm leads to an 85% enhancement of damping-like torque efficiency compared to the reference sample with a Pt layer as the spin source. These results demonstrate orbital angular momentum transport as an efficient torque-generation mechanism in synthetic antiferromagnetic heterostructures, offering a scalable route toward low-power spintronic devices.

Spin-orbit torque (SOT) has become a promising technique for energy-efficient magnetisation switching in spintronic devices. Efforts have focused on using various materials, including metals, alloys, topological insulators, and 2D materials, to boost the efficiency of SOT switching[1–5]. Meanwhile, the industry favours perpendicular magnetic anisotropy (PMA) systems for their compactness and thermal stability in memory applications[1,2,6]. However, achieving deterministic SOT switching in PMA systems still requires an in-plane magnetic field to break symmetry, which increases power consumption and limits practical use[7–12]. As a result, ongoing research focuses on achieving field-free switching. Approaches such as interlayer exchange coupling, tilted magnetic anisotropy, and antiferromagnetic seed layers have been investigated to enable field-free switching[13–23]. Despite substantial progress, a solution fully compatible with industrial requirements has yet to be realised.

From another perspective, orbital torque (OT) has recently emerged as a promising alternative to SOT, offering potential advantages for improved energy-efficiency[24–26]. In these systems, orbital torques can be generated through the orbital Hall effect (OHE). Analogous to the spin Hall effect (SHE), OHE generates a transverse flow of orbital angular momentum when an electric field is applied to certain non-magnetic (NM) layers[26–29]. However, the orbital current cannot directly interact with the magnetisation of the commonly used ferromagnetic materials. Therefore, the orbital current generated in the NM layer must first be converted into a spin current via spin-orbit coupling before exerting a torque on the adjacent ferromagnet[30–35].

Materials with a strong OHE, such as certain transition metals and oxides, can provide an additional mechanism to manipulate magnetic order, potentially surpassing the efficiency of conventional SHE-based devices[27,32,34,36–38]. However, the experimental demonstration of the advantages of OT over SOT remains limited. In addition, few studies have explored OT to enhance the field-free switching efficiency at room temperature. Bridging this gap, both in fundamental understanding and device implementation, could enable a new class of low-

[1]School of Physical and Mathematical Sciences, Nanyang Technological University, 21, Nanyang Link, Singapore. [2]Institute of Physics, Johannes Gutenberg University Mainz, Mainz, Germany. [3]These authors contributed equally: Bilal Jamshed, Subhakanta Das. ✉e-mail: prem@ntu.edu.sg

power, scalable spintronic memory and logic devices. In this work, we utilised the spin-reorientation mechanism in Co/Ru/[Co/Pt]$_3$ heterostructures - achieved via synthetic antiferromagnetism—to achieve field-free magnetisation switching in perpendicular magnetic anisotropy samples, driven by OT.

Synthetic antiferromagnets (SAFs) are magnetic layered structures comprising at least two FM layers coupled antiferromagnetically through a non-magnetic spacer[39–41]. SAF structures minimise stray fields, enabling higher-density chip integration. Sbiaa et al. showed magnetisation reorientation from in-plane to out-of-plane in an SAF stack comprising a Co thin film and Co/Pd multilayers[42]. Ranjbar et al. reported magnetisation reorientation for a Co sublayer thickness as large as 1 nm in Co/Pd multilayers[43]. However, in those studies, spin reorientation was reported as an observation but was not utilised for any specific application. Moreover, the spin reorientation was not observed for a Co thickness exceeding ~ 1 nm.

In our SAF structure, the synergistic effect of exchange coupling mediated via the Ru spacer layer and perpendicular magnetic anisotropy achieved through the [Co/Pt]$_3$ multilayers leads to the spin reorientation in the bottom Co layer. By tuning the bottom Co-layer thickness (t_{Co}), we identify an optimal thickness regime (t_{Co} = 1.1 to 1.4 nm) that enables field-free switching. Through micromagnetic simulations and experiments on three series of samples (A-C), we show that the spin reorientation generates an in-plane magnetisation component that effectively breaks the symmetry for deterministic switching without an external magnetic field. Series D samples without SAF further clarify the contribution of Ru to OT and the role of SAF in enabling field-free switching. Engineering an appropriate SAF stack with optimised FM and spacer thickness can thus facilitate field-free switching.

Results

Optimisation of Spin-reorientation

Our first series of samples (series A) has the stack structure Si/SiO$_2$/Ta(2)/NiW(2)/Ru(3)/Pt(2)/Co(t)/Ru(1.1)/[Co(0.5)/Pt(0.8)]$_3$/Pt(1.2) (Fig. 1a), deposited via DC/RF magnetron sputtering. The role of the Ta(2) seed layer is to promote PMA at the Co/Pt interface and to improve adhesion to the substrate, and NiW(2) is used to enhance the

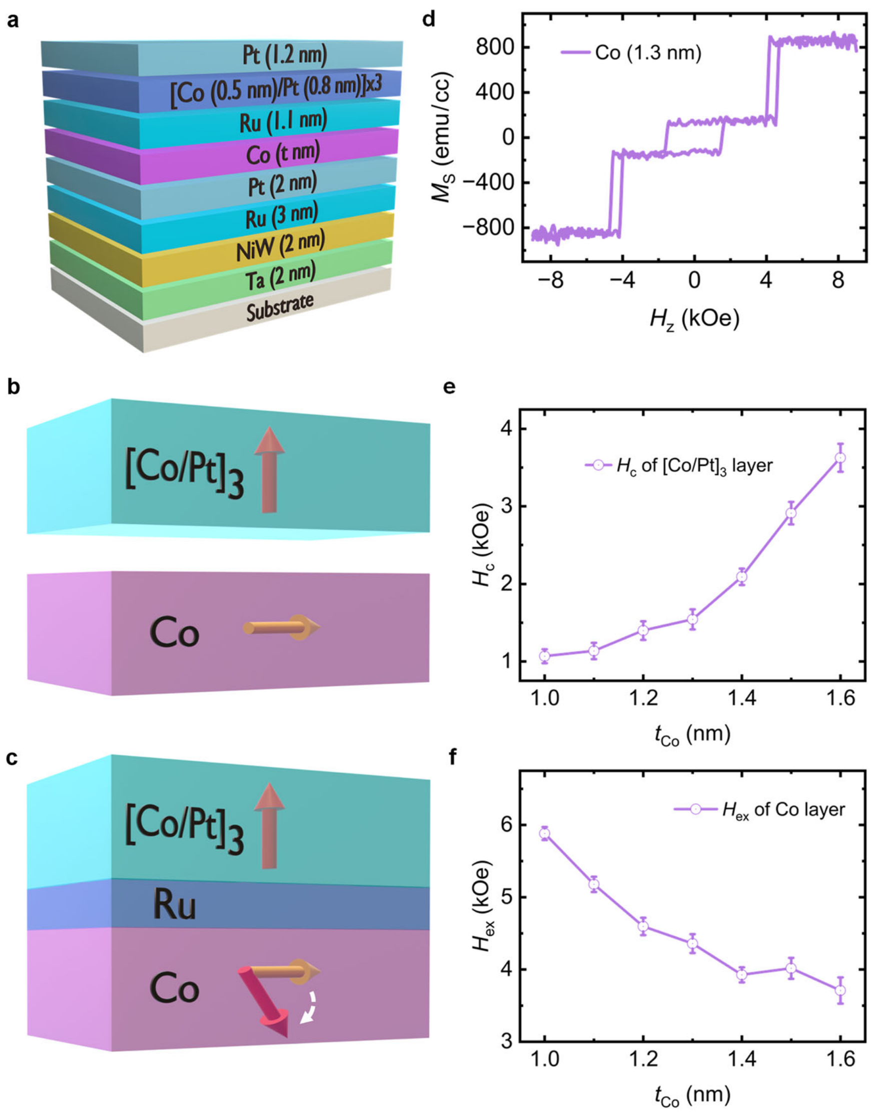

Fig. 1 | Thin-film characterisation. a Schematic illustration of Series A samples. **b** Without the Ru spacer layer, the two ferromagnetic layers would have perpendicular and in-plane magnetic moments. **c** In the presence of a 1.1-nm Ru spacer layer, the competition between the RKKY coupling and shape anisotropy leads to the spin reorientation in the bottom ferromagnetic layer. **d** Hysteresis loop of sample with t_{Co} = 1.3 nm, measured via VSM in the out-of-plane (OOP) direction. **e** Coercivity (H_c) of [Co/Pt]$_3$ and **f** Exchange field (H_{ex}) of Co multilayers for t_{Co} from 1.0 nm to 1.6 nm. Error bars represent estimated uncertainties derived from the measurement range and the magnetic field resolution (step size).

crystallinity of Ru[44]. The bottom Co thickness was varied from 1 to 2 nm in increments of 0.1 nm. The idea behind this series is to investigate the Co thickness that gives the optimum spin reorientation effect (see supplementary Note 1). To determine the Ru thickness for optimum exchange coupling, we varied the Ru thickness from 0.5 nm to 2.0 nm (see supplementary Note 2). There is no Ruderman-Kittel-Kasuya-Yosida (RKKY) coupling between Co and $[Co/Pt]_3$ when there is no Ru (Fig. 1b). Although Ru (0.5 nm) gives the largest coupling, we chose Ru (1.1 nm) layer as the optimum spacer layer for switching performance, to balance spin-reorientation and exchange coupling (Fig. 1c). The Ru (3 nm) layer, sandwiched between NiW (2 nm) and Pt (2 nm), is used as the orbital Hall layer to generate orbital current. The Pt (2 nm) is used for orbital-to-spin current conversion layer to induce magnetisation switching of the ferromagnetic layer at the top. As Ru exhibits higher electrical conductivity than Pt, increasing the Ru thickness (shown later in series B samples) leads to preferential current flowing through the Ru layer due to its lower resistivity. This redistribution of charge current reduces the effective current density in Pt and suppresses its intrinsic spin Hall torque contribution[44]. Nevertheless, Pt remains essential as a strong spin-orbit coupling layer that converts the orbital Hall current generated in Ru into a spin current within the Pt layer, which is then injected into the FM layers. Accordingly, the total spin-orbit torque acting on the ferromagnet can be written as

$$\tau_{total} = \tau_{Ru}^{OHE \rightarrow SHE} + \tau_{Pt}^{SHE}$$

where $\tau_{Ru}^{OHE \rightarrow SHE}$ denotes the torque arising from the orbital Hall current generated in Ru and converted into spin current in Pt, and τ_{Pt}^{SHE} represents the torque generated directly by the spin Hall effect in Pt. Consequently, with increasing Ru thickness, the net spin-torque is expected to become increasingly dominated by the Ru-derived orbital Hall contribution, while the direct Pt spin Hall torque plays a secondary, additive role.

The magnetic properties of all the films were investigated using a polar magneto-optic Kerr effect (p-MOKE) microscope and a vibrating sample magnetometer (VSM). We present the hysteresis loops obtained from the VSM measurements of the SAF sample with t_{Co} = 1.3 nm in Fig. 1d to provide a clear visualisation (see supplementary note 1 for the hysteresis loops of the remaining samples). The M-H loops of t_{Co} = 1.3 nm sample show that $[Co/Pt]_3$ exhibits a perpendicular magnetic anisotropy (PMA) with coercivity (H_c) values of 1543 Oe. The bottom Co layer is antiferromagnetically coupled and exhibits switching at about 4.4 kOe in the sample with t_{Co} = 1.3 nm. Figure 1e, f represent the H_c and exchange field (H_{ex}) as a function of t_{Co}, respectively. In contrast, for the t_{Co} = 1.8 nm sample, there is a strong slope at zero field, indicating that the magnetisation is not reoriented completely in the perpendicular direction. For the details of the other samples, please refer to the supplementary Note 1.

We fabricated devices using photolithography and ion milling after thin-film characterisations. The spin reorientation in the SAF samples depends on the shape anisotropy and RKKY coupling between the two FM layers. Therefore, instead of making + shaped Hall bars of magnetic material, we patterned long devices of FM material with overlapping electrodes to maintain the spin reorientation consistent throughout the device (Fig. 2a). We performed magnetic and transport measurements on the Hall bar devices to characterise the SOT switching efficiency of SAFs.

Current-induced magnetisation switching

We performed magnetisation switching by applying constant current pulses on Hall bar devices with lateral dimensions of 20 µm × 100 µm (Fig. 2a). Figure 2b, c show the magnetisation switching from $+m_z$ to $-m_z$ and $-m_z$ to $+m_z$, respectively, after applying a current pulse of 66 mA for 50 µs in the absence of an external magnetic field for t_{Co} = 1.3 nm. The reference Kerr microscopy image was obtained immediately after saturating the sample with an external out-of-plane magnetic field (H_z) of ±4000 Oe. The Kerr image, for switching investigations, was obtained after applying the current pulse in the absence of any external field. A clear magnetisation switching to the $-m_z$ state (Fig. 2b) and $+m_z$ state can be seen in Fig. 2c. However, we did not observe $-m_z$ to $+m_z$ switching simply by changing the polarity of the current direction. Conversely, when we saturated the device in the $-m_z$ direction (H_z = −4000 Oe), the applied current switched the magnetisation from $-m_z$ to $+m_z$. This dependence on current polarity confirmed that the magnetisation switching occurred due to the spin-orbit torque. We performed these measurements in all the series A samples and observed field-free switching for t_{Co} = 1.1, 1.2, 1.3, and 1.4 nm samples. A similar experiment performed on a 10 µm × 100 µm Hall bar device likewise exhibits robust field-free switching (supplementary note 6). Samples with a Co thickness thinner than 1 nm or thicker than 1.5 nm did not show field-free switching.

Further, we studied the current-induced magnetisation switching (CIMS) by sweeping direct current (DC) pulses and measuring the anomalous Hall resistance on all the samples with t_{Co} = 1.0 to 1.6 nm at H_x = 0 Oe, as shown in Fig. 2d. Consistent with the results obtained from constant DC pulse measurements, we observed field-free magnetisation switching in series A samples with t_{Co} = 1.1, 1.2, 1.3, and 1.4 nm, as shown in Table 1. Along with this, we have performed a Joule heating experiment on the sample with t_{Co} = 1.3 nm to rule out the effect of Joule heating on magnetisation switching (please see the supplementary note 6).

We calculated the difference in the Hall resistance (ΔR_{AHE}) between up and down magnetisation states by sweeping an external out-of-plane magnetic field from AHE measurements (supplementary Note 3). Further, we calculated the switching percentage using the formula $\Delta R_H / \Delta R_{AHE} \times 100\%$, where ΔR_{AHE} is the anomalous Hall resistance change measured under an applied out-of-plane field (H_z), and ΔR_H is measured by sweeping current in the absence of H_x. The values of ΔR_{AHE} and ΔR_H are given in Table 1. We observed a maximum field-free switching percentage of 96% in the SAF sample with t_{Co} = 1.3 nm. The critical switching current density was calculated at the midpoint of the Hall resistance transition of the ΔR_H-J_c loops. The variation of field-free switching percentage and critical switching current density with t_{Co} is shown in Fig. 2e. Further, we performed the CIMS experiment as a function of in-plane magnetic fields to show 100% magnetisation switching in the presence of H_x (Fig. 2f).

The robust field-free switching originates from the interplay between interfacial magnetic anisotropy, RKKY exchange coupling, and shape anisotropy. For smaller Co thicknesses, interfacial magnetic anisotropy arising from the Pt/Co interface (K_s/t_{Co}) (here K_s is the surface anisotropy energy density), and the antiferromagnetic coupling (AFC) energy together dominates over shape anisotropy, enforcing an out-of-plane magnetisation with antiparallel alignment driven by RKKY coupling. As the Co thickness increases, K_s/t_{Co} decreases, and the shape anisotropy progressively tilts the magnetisation away from the antiparallel direction. For intermediate thickness values (optimum regime), the magnetisation tilt produces both out-of-plane and in-plane components of M. At higher thickness (> 1.8 nm), the bottom Co layer has a larger in-plane component. In the optimised regime, the resulting canted magnetisation effectively breaks symmetry, enabling deterministic field-free switching. However, once the in-plane component becomes too strong at larger thicknesses, this symmetry-breaking mechanism is lost, and field-free switching is no longer observed. Due to the reduced RKKY coupling (reduced $J^*cos\theta$), the $[Co/Pt]_n$ layers do not switch, and deterministic switching between ±z states is lost, requiring an external field to define the switching direction. We have performed micromagnetic simulations using MuMax3 to deepen the understanding, to demonstrate the spin-reorientation mechanism, and to explain the field-free switching. Details of the

 https://doi.org/10.1038/s41467-026-72894-8

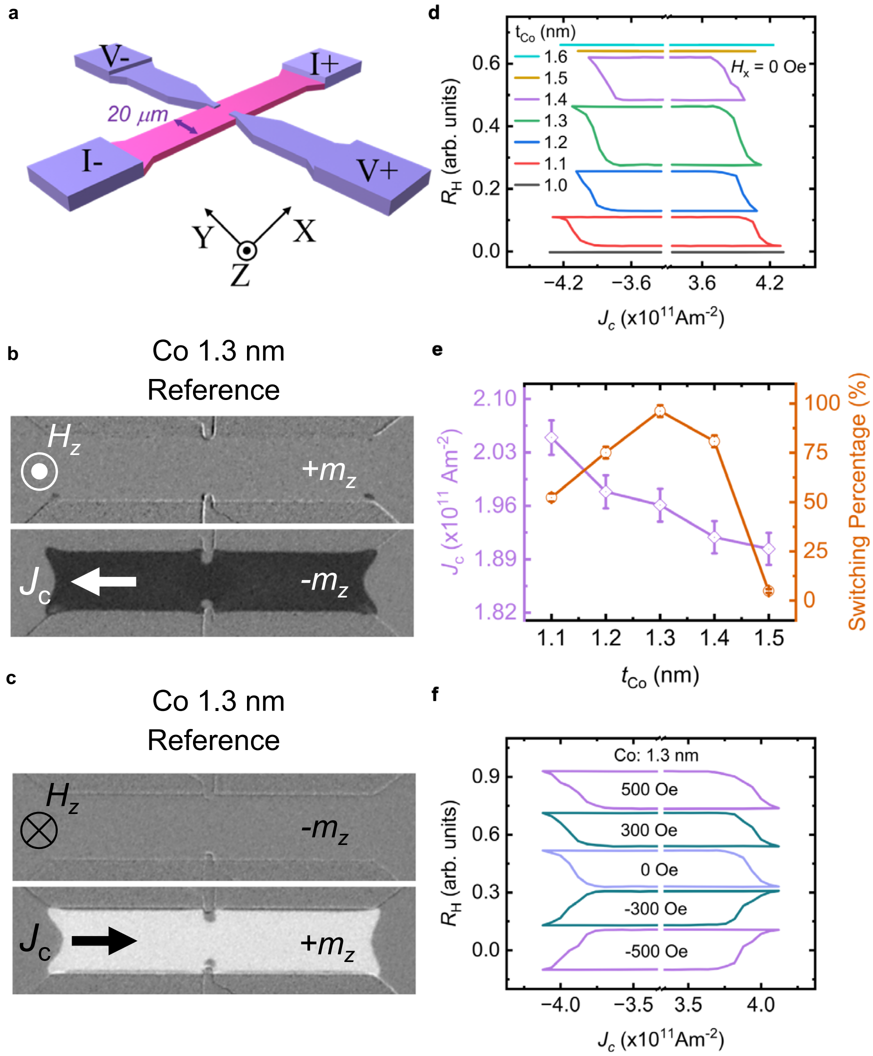

Fig. 2 | Field Free Switching measurements on series A samples. **a** The schematic illustration of the device, **b** The magnetisation switching from $+m_z$ to $-m_z$ direction in the sample with a Co thickness of 1.3 nm. The image at the top (grey) represents the initial saturated state ($+m_z$). The bottom image represents the magnetisation ($-m_z$) of the device after applying current pulses. **c** Magnetisation switching from $-m_z$ to $+m_z$ direction. **d** The anomalous Hall resistance, representing current-induced magnetisation switching (or its absence) in samples with Co thicknesses ranging from 1.0 to 1.6 nm. It is noticed that the samples with Co thickness ranging from 1.1 nm to 1.4 nm exhibit field-free switching. **e** The critical current density and the switching percentage for all Co thicknesses. **f** R_H of series A sample with 1.3 nm thick Co for various in-plane magnetic fields. Error bars represent estimated uncertainties combining the measurement range and the current density resolution (step size).

simulation methodology and results are provided in supplementary note 9.

Furthermore, we performed angular-dependent anomalous Hall effect (AHE) measurements on samples with varying Co thickness to quantitatively probe the presence of an in-plane magnetisation component. Hall bar devices with dimensions of 20 μm × 100 μm were employed, and a DC of 100 μA was applied to measure the anomalous Hall voltage (V_{AHE}). An external H_z was swept while an in-plane field H_x = 100 Oe was applied at an azimuthal angle (φ) relative to the applied DC, and φ was varied from 0° to 360° in steps of 30°. Figure 3a shows representative AHE loops for a device with t_{Co} = 1.3 nm measured at $\varphi = 30^{\circ}$ and 210°, revealing a clear loop shift for opposite in-plane field directions. The shift was quantified as $\Delta H = (H_1 + H_2)/2$, where H_1 and H_2 are the switching fields. Figure 3b presents the azimuthal dependence of ΔH for t_{Co} = 1.0-1.5 nm. For t_{Co} = 1.0 and 1.5 nm, ΔH remains small and symmetric, whereas samples with t_{Co} = 1.2–1.4 nm exhibit a pronounced asymmetry, with the polar plots shifted toward the +x direction. This behaviour confirms the presence of a finite in-plane magnetisation component. The sinusoidal dependence of ΔH on φ, clearly visible in Fig. 3c, is indicative of spin canting and directly reflects the in-plane symmetry breaking in the system[16,45]. A finite angle is essential to resolve the angular dependence of ΔH; in the limiting case of $H_x = 0$, the angular variation (and thus its sinusoidal dependence) cannot be meaningfully extracted.

We also performed a similar experiment for the existence of an in-plane magnetisation component. The sample was first saturated by applying a large in-plane magnetic field in the positive direction, followed by current-sweeping anomalous Hall effect (AHE) measurements. The same procedure was then repeated after saturating the sample in the negative direction. This protocol verified the presence of a finite in-plane magnetisation component at zero applied in-plane field. If such a component exists, the polarity of the AHE loop is expected to reverse depending on the initial saturation direction. To test this, in-plane magnetic fields of ±3200 Oe were applied, and the corresponding AHE responses were recorded. As shown in Fig. 3d, the observed reversal of the AHE loop polarity provides direct evidence for the existence of an in-plane magnetisation component.

 https://doi.org/10.1038/s41467-026-72894-8

Orbital Hall effect optimisation

Having shown field-free switching based on SAF in an orbital Hall layered system, we investigated another series of samples by varying the Ru thickness (t_{Ru} = 0, 3, 5, 7, 10 nm) to enhance the orbital torque and study its influence. The series B samples consist of the stack structure - Si/SiO$_2$/Ta(2)/NiW(2)/Ru(t)/Pt(2)/Co(1.3)/Ru(1.1)/[Co(0.5)/Pt(0.8)]$_3$/Pt(1.2) (Fig. 4b). The bottom Co layer thickness is fixed at 1.3 nm for all the series B samples, corresponding to the sample in series A where we observed a maximum field-free switching of 96% (Fig. 2e). Here, we used Ru(t) as the orbital Hall layer, as Ru has been theoretically reported and experimentally verified to have a strong orbital Hall conductivity[24,29,44]. In this setup, the bottom Pt layer acts as an intermediary layer that converts the orbital current (I_{OH}) into spin current (I_{SH}), which then interacts with the magnetisation of the Co layer to induce magnetisation switching (Fig. 4a). We performed VSM and MOKE measurements, following similar methods discussed for series A samples, to characterise the magnetic properties of all the samples. M-H loops of series B samples are shown in Fig. 4c. The H_c of Co/Pt multilayers and the H_{ex} of Co layers show an increase with the increase in t_{Ru} (Fig. 4e, f). Such results are expected based on the crystalline texture improvement of the Ru layer.

We performed X-ray diffraction (XRD) measurements using a Rigaku SmartLab XRD system to characterise the crystal structure of our samples with t_{Ru}. We observed the XRD peaks corresponding to the Co/Pt multilayers and the Ru layer to coincide with each other for all the samples. The shift of the XRD peak from 41.45° to 41.73° with increasing t_{Ru} suggests an improvement in the Ru layer crystallinity and/or Co/Pt multilayer interface[44,46,47]. We also observed that the XRD peak of the Co layer shifted from 43.28° to 42.73° with increasing t_{Ru}, similar to our previous reported work by Bhatti et al.[48]. For further information on XRD results, please refer to the supplementary note 4.

We performed a similar current-induced magnetisation switching experiment on series B samples. All samples showed a clear field-free switching by sweeping the direct current pulses (Fig. 5a). Additionally, we performed the experiments with varying in-plane magnetic fields to show 100% magnetisation switching (Fig. 5b). The reduced switching Hall resistance in Fig. 5b at ±300 Oe originates from partial compensation between the SAF-induced intrinsic in-plane field and the externally applied assisting field, which weakens chirality selection and stabilises a mixed multidomain state. At higher assisting fields (±500 Oe), the external field dominates, restoring deterministic switching and increasing ΔR_H.

We also investigated the field-free switching of a reference sample with Pt (5 nm) as the spin Hall layer, which is the most commonly used element in spintronics. This sample showed a lower J_c in comparison to a sample with no Ru. However, when the Ru thickness was increased, we observed a monotonic reduction in critical current density,

Table 1 | Hall resistances and switching efficiency as a function of t_{Co}

t_{Co} (nm)	ΔR_{AHE} (Ω)	ΔR_H (Ω) @ 0 Oe	% Switching (ΔR_H /ΔR_{AHE})%	Efficiency (×10^{-10}m^{2}A^{-1})
1.0	0.3080	–	–	–
1.1	0.3135	0.1640	52.31	2.55
1.2	0.2818	0.2113	75.1	3.79
1.3	0.1954	0.1880	96.2	4.81
1.4	0.1811	0.1463	80.8	4.13
1.5	0.2077	0.01016	4.89	0.25
1.6	0.1770	–	–	–

Here, ΔR_{AHE} and ΔR_H represent the change in AHE resistance measured by sweeping the field and current, respectively. Efficiency is defined as %switching/critical current density.

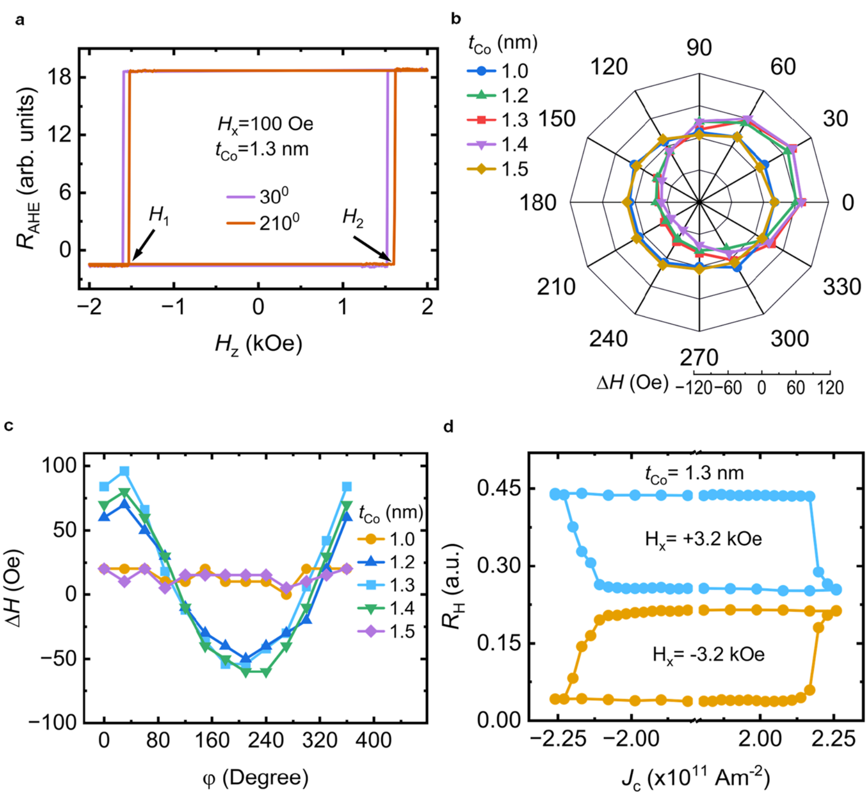

Fig. 3 | Angle-dependent AHE measurements. a AHE loop for angles 30° and 210° shows a shift. **b** The shift in the polar loop for various thicknesses of the Co layer. **c** angle dependency of the shift. **d** The change of polarity of the loop occurred when the in-plane component of canted magnetisation was saturated under large in-plane magnetic fields of two different signs.

https://doi.org/10.1038/s41467-026-72894-8

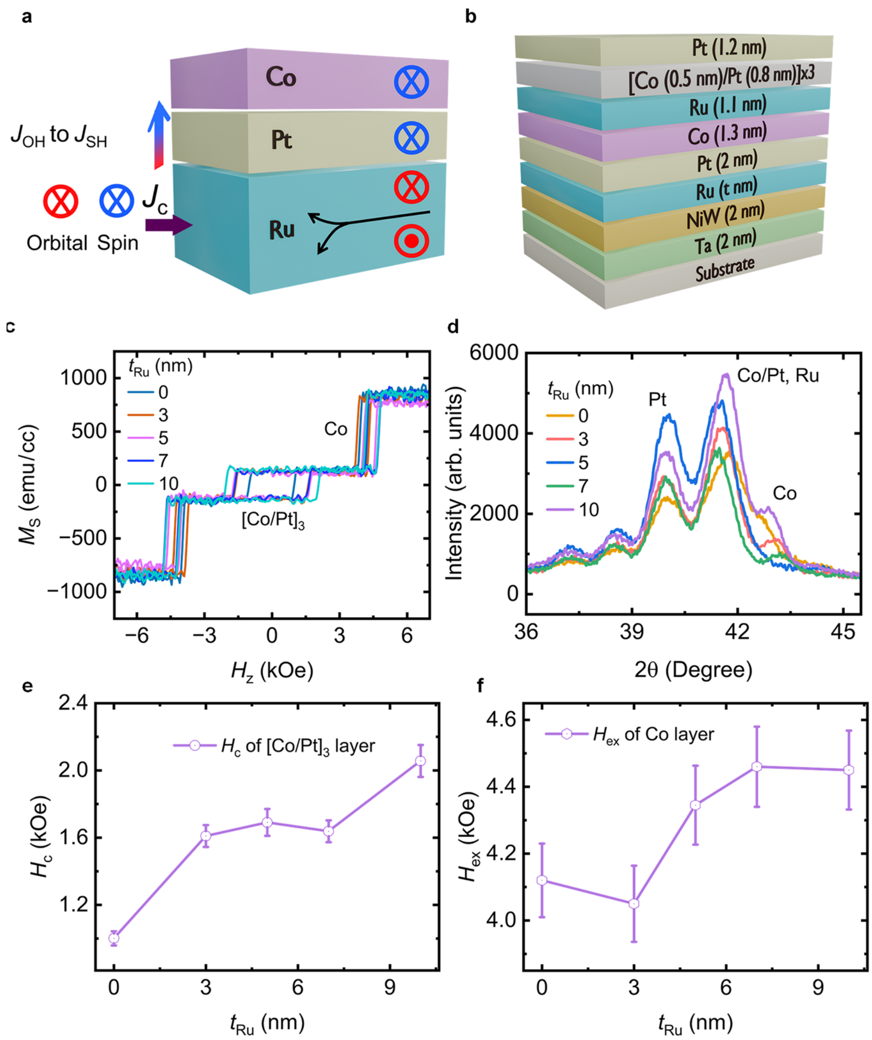

Fig. 4 | Orbital Hall effect enhancement. a The schematic Illustration of orbital current generation in the Ru layer and conversion from orbital to spin current in the Pt layer. **b** The SAF stack structure with varying thicknesses of Ru layer. **c** The M-H loops - captured using VSM in the out-of-plane (OOP) direction- for various Ru thicknesses in samples with a bottom layer of Co 1.3 nm. **d** The XRD data for various Ru thickness values. **e**, **f** H_c of Co/Pt and H_{ex} of Co layer for t_{Ru} ranging from 0 nm to 10 nm for series B samples. Error bars represent estimated uncertainties derived from the measurement range and the magnetic field resolution (step size).

indicating the role of orbital torque arising from Ru. We also calculated the critical current density through Ru/Pt layers using a parallel conductance model, taking into account the resistivities of individual layers and the current shunting effect (please refer to supplementary Notes 7, 8). The maximum percentage reduction in the critical density through the stack is 12% for $t_{Ru} = 10$ nm (Fig. 5c). Most samples with $t_{Ru} > 3$ nm exhibited a field-free switching percentage of over 90% (Fig. 5d). The samples with Ru as the orbital Hall layer (series B samples) showed a clear reduction in switching current density relative to the reference sample (Fig. 5d).

Again, we calculated the orbital torque-driven magnetisation switching efficiency (switching percentage per unit critical current density) for all the samples (Fig. 5e). We quantified the relative efficiencies of SHE-driven switching to the orbital-torque-assisted switching by taking the ratios of switching efficiency of samples with no Ru (Ru(0)/Pt(2) and Ru(0)/Pt(5)) to the samples with $t_{Ru} = 10$ nm. The ratio of orbital-assisted switching to SOT-based switching efficiencies was approximately 1.32 and 1.25, respectively. These values indicate that the insertion of the Ru orbital Hall layer enhances the switching efficiency by up to ~25% compared to pure SHE-driven systems, consistent with the presence of an additional orbital torque contribution. Moreover, we applied constant current pulses with opposite polarity to show that the history of the in-plane magnetic field does not affect field-free switching (Fig. 5f), suggesting that our samples can be implemented in memory devices and undergo large repetitions of read-write cycles. We also deposited another set of samples (series C) in which the Ru layer was deposited on top of the Co/Pt multilayers, and we observed the same reduction in critical current density with increasing t_{Ru}. (For further information, please refer to supplementary Note 5).

Furthermore, we have calculated the damping-like torque efficiency (ξ_{DL}^{E}) as a function of t_{Ru} to elucidate the role of the Ru layer in the reduction of critical switching current density. For this purpose, we have deposited a new series of samples (series D) without SAF: Si/SiO2/Ta(1)/Pt(1)/[Co(0.5)/Pt(0.8)]$_{x3}$/Pt(1.2)/Ru(t), where $t_{Ru} = 0, 3, 5, 7, 10, 15,$ 20 and 30 nm, as shown in Fig. 6a. This stack eliminates the influence of SAF, NiW seedlayer and uses thin layers of Ta and Pt, mainly for adhesion and achieving PMA. Such a stack reduces the complexity in series A, B, and C and helps us to isolate and focus on the role of Ru clearly. Pt(2 nm) at the top serves as an orbital to a spin current converter.

We carried out anomalous Hall voltage (AHV) loop shift measurements on Hall bar devices with lateral dimensions of 20 µm × 100 µm to calculate the ξ_{DL}^{E} [44,46–51]. Figure 6b shows an optical

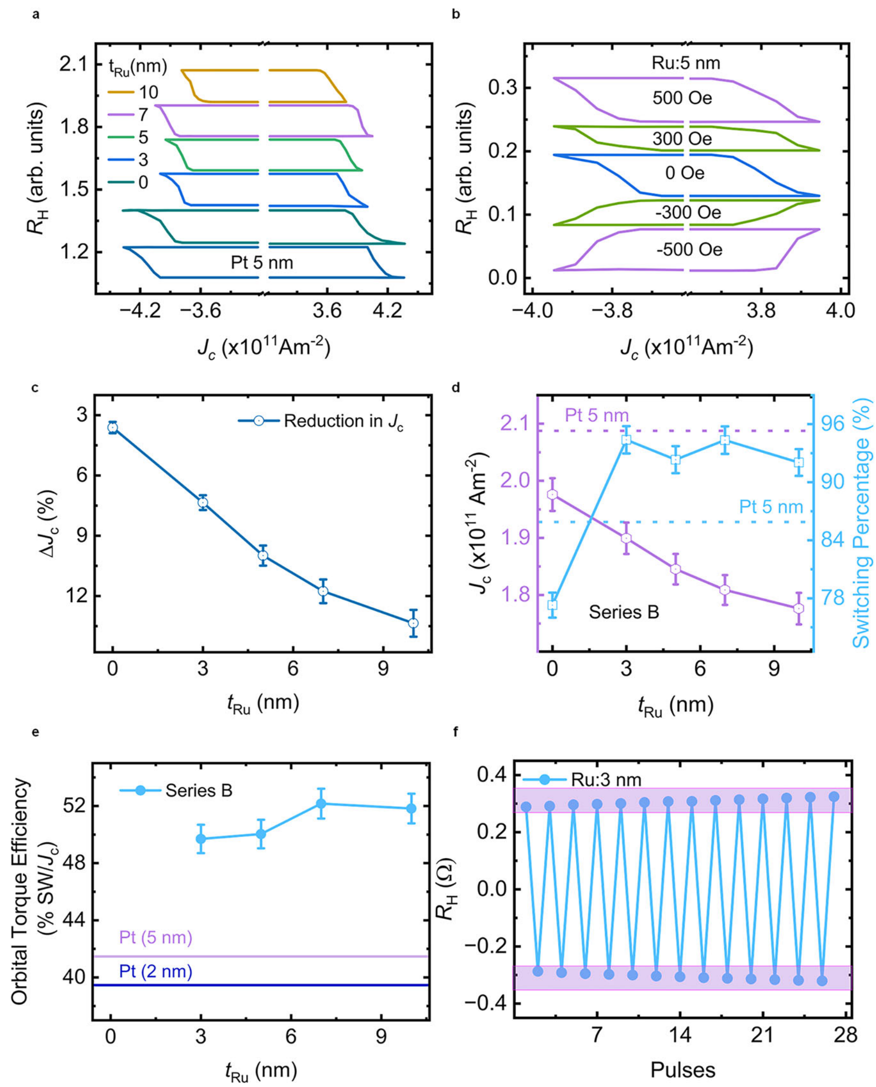

Fig. 5 | Effect of Ru layer thickness on current-induced magnetisation switching. **a** Field-free R_H-J_c data for various Ru thicknesses along with the reference sample (dark blue), showing a significant decrease in the current density with t_{Ru}. **b** current-induced magnetisation switching of the $t_{Ru} = 5$ nm sample with varying H_x. **c** The reduction in the critical current density through the stack with respect to the Ru thickness, **d** critical current density through the stack and switching percentage, **e** switching efficiency against Ru thickness, and **f** multiple current pulses with opposite polarity applied to the sample with $t_{Ru} = 3$ nm, demonstrating repeatability switching of the sample. Error bars represent estimated uncertainties combining the measurement range and the current density resolution (step size).

microscopic image of the device with a schematic of the electrical setup. Constant DC pulses and an in-plane magnetic field were applied along the longitudinal direction, and the Hall voltage was recorded as a function of H_z. These samples - because of the absence of SAF-do not show field-free switching, further confirming the role of SAF in field-free switching. Figure 6c shows representative data for the-sample with $t_{Ru} = 10$ nm at $I_{DC} = \pm 17$ mA and $H_x = 2800$ Oe. A distinct shift in the normalised AHV loop was observed, and it can be attributed to an effective out-of-plane field generated from the SOT (H_{SOT}). We calculated H_{SOT} by taking the mean value of the switching fields $\left[\left(H_{SW}^{\uparrow-\downarrow} + H_{SW}^{\downarrow-\uparrow}\right)/2\right]$ (up-to-down, $H_{SW}^{\uparrow-\downarrow}$ and down-to-up, $H_{SW}^{\downarrow-\uparrow}$) for each I_{DC} and performed a linear regression to calculate the slope H_{SOT}/I_{DC}. The opposite linear dependency of H_{SOT} upon I_{DC} by switching the polarity of H_x and nearly zero H_{SOT} in the absence of H_x-satisfies the criteria of the SOT mechanism. This behaviour originates from the opposite alignment of domain wall magnetisation in the Co layer[52].

Next, we calculated the SOT efficiency (current-induced effective field per unit electric field, H_{SOT}/E) as a function of H_x, where E is the electric field applied to the device. We used the SOT efficiency to calculate the saturation damping-like torque efficiency $\left(\xi_{DL}^{E}\right)$ using the formula

$$\xi_{DL}^{E} = \frac{2e}{\hbar} M_s t_{FM} \left(\frac{\mu_0 H_{SOT}}{E}\right) \tag{1}$$

Where e is the electronic charge, $\hbar$ is the reduced Planck's constant, μ_O is the free space magnetic permeability, M_s and t_{FM} are the saturation magnetisation and thickness of the magnetic layer, respectively. We observed negative values for ξ_{DL}^{E} for this series. The Ru layer on top of the Co/Pt surface generates an I_{OH} in the Ru layer and is converted to an I_{SH} via the top Pt layer. As the Ru and Pt are placed above the FM layer, they have negative orbital and spin Hall conductivities, respectively. Thus, the net SOT effect in samples is a negative ξ_{DL}^{E} contribution. Figure 6d shows the values of ξ_{DL}^{E} for all the thicknesses of the Ru. We observed that the $|\xi_{DL}^{E}|$ shows an enhancement of 1.9 times via OHE compared to the reference sample in which only SHE is present (2 nm Pt layer).

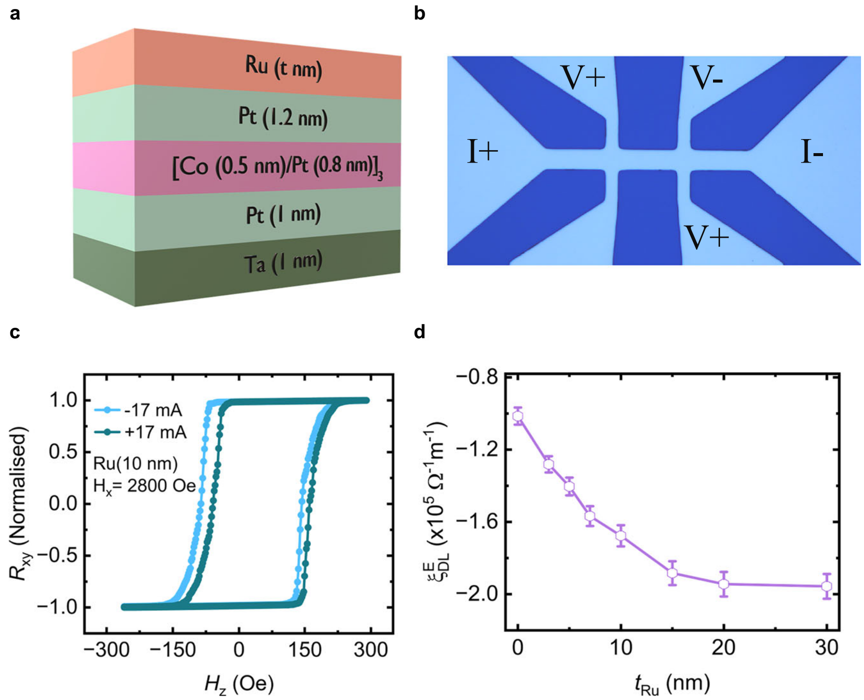

Fig. 6 | Damping-like torque efficiency measurements in series D. a Schematic of the stack structure used for the calculation of the damping-like torque contribution. **b** Optical microscopic image of the fabricated Hall cross device. The electrical measurement configuration is overlaid, with the current injection path and transverse voltage detection channels indicated in white as ±*I* and ±*V*, respectively. **c** Normalised anomalous Hall voltage (AHV) hysteresis loops for the Ru (10 nm) sample measured under $I_{DC} = \pm 17$ mA in the presence of an in-plane bias H_x. The observed current-dependent shift of the AHV loops is subsequently used to calculate the damping-like torque efficiency. **d** Comparison of the saturated damping-like torque efficiency (ξ^E_{DL}) for all investigated samples. A systematic increase in $|\xi^E_{DL}|$ is observed with increasing Ru thickness, indicating an enhancement of the damping-like torque efficiency. The trend suggests that the orbital Hall effect in Ru becomes stronger with increasing thickness and saturates at a thickness of 15 nm. Error bars represent the standard deviation of the measured values.

In summary, we have demonstrated low-current, field-free magnetisation switching in orbital torque (OT) systems by exploiting spin reorientation induced via synthetic antiferromagnetism (SAF). Spin-reorientation was tuned by varying the Co layer thickness (t_{Co}) from 1.0 to 1.8 nm, and we observed field-free switching within the range of 1.1-1.4 nm, reaching a maximum switching percentage of 96% and peak switching efficiency at $t_{Co} = 1.3$ nm. Separately, we tuned the thickness of the Ru orbital Hall (OH) layer between 3 and 10 nm to enhance the orbital current injection. Additional experiments in stacks without SAF confirmed the dominant orbital contribution of Ru. Damping-like torque was enhanced by 1.9-fold compared to the reference sample (Pt 2 nm). The sample with $t_{Ru} = 10$ nm exhibited a 12% reduction in critical switching current density through the stack and a 25% increase in switching efficiency compared to reference spin-orbit torque (SOT) devices. This innovative approach offers a promising pathway for developing next-generation, energy-efficient spintronic memory and logic devices.

Methods

Device fabrication, Thin-films and electrodes deposition

The SAFs were fabricated in high-vacuum magnetron sputtering equipment onto thermally oxidised silicon substrates. The base chamber pressure was maintained below 3.0×10^{-8} Torr, and the deposition was carried out at room temperature. Throughout the deposition process, substrates were rotated at 40 revolutions per minute to ensure film uniformity.

All layers were deposited using a direct current magnetron sputtering system at a working argon gas pressure of 3 m Torr and a sputtering power of 50 W. Device patterning, including Hall bar and straight wire geometries, was accomplished using photolithography, followed by argon ion-beam etching. Then, electrical contact pads were prepared using a Ta(5)/Cu(90)/Ta(5) trilayer deposition.

Hall effects measurements

To enable Hall resistance measurements, samples were attached to a printed circuit board (PCB) using a wire-bonding machine. Room-temperature Hall resistance measurements were carried out using a calibrated Quad electromagnet setup. Current pulses were supplied with a Keithley 6221 source. For field-dependent Hall resistance measurements, a direct current of 0.1 mA was applied. For the investigation of current-induced magnetisation switching, current pulses with 10 μs duration were used.

Data availability

The data supporting the findings in this study are provided in the main text and Supplementary Information. The data are openly available in the NTU research data repository DR-NTU (Data) at https://doi.org/10.21979/N9/00DPTQ.

References

1. Shao, Q. et al. Roadmap of Spin–Orbit Torques. *IEEE Trans. Magn.* **57**, 1–39 (2021).
2. Bhatti, S. et al. Spintronics based random access memory: a review. *Mater. Today* **20**, 530–548 (2017).
3. Ji, G., Zhang, Y., Chai, Y. & Nan, T. Recent progress on controlling spin-orbit torques by materials design. *Npj Spintron* **2**, 56 (2024).
4. Han, X., Wang, X., Wan, C., Yu, G. & Lv, X. Spin-orbit torques: materials, physics, and devices. *Appl. Phys. Lett.* **118**, 120502 (2021).
5. Kallinatha, H. D., Rai, S. & Talawar, B. A detailed study of SOT-MRAM as an alternative to DRAM primary memory in a multi-core environment. *IEEE Access* **12**, 7224–7243 (2024).
6. Manchon, A. et al. Current-induced spin-orbit torques in ferromagnetic and antiferromagnetic systems. *Rev. Mod. Phys.* **91**, 035004 (2019).

7. Mihai Miron, I. et al. Current-driven spin torque induced by the Rashba effect in a ferromagnetic metal layer. *Nat. Mater.* **9**, 230–234 (2010).
8. Fukami, S., Anekawa, T., Zhang, C. & Ohno, H. A spin–orbit torque switching scheme with a collinear magnetic easy axis and current configuration. *Nat. Nanotechnol.* **11**, 621–625 (2016).
9. Gambardella, P. & Miron, I. M. Current-induced spin–orbit torques. *Philos. Trans. R. Soc. Math. Phys. Eng. Sci.* **369**, 3175–3197 (2011).
10. Manchon, A. & Zhang, S. Theory of spin torque due to spin-orbit coupling. *Phys. Rev. B* **79**, 094422 (2009).
11. Safeer, C. K. et al. Spin–orbit torque magnetization switching controlled by geometry. *Nat. Nanotechnol.* **11**, 143–146 (2016).
12. Wang, K., Qian, L., Ying, S.-C. & Xiao, G. Spin-orbit torque switching of chiral magnetization across a synthetic antiferromagnet. *Commun. Phys.* **4**, 10 (2021).
13. Fan, H. et al. Field-free switching and high spin–orbit torque efficiency in Co/Ir/CoFeB synthetic antiferromagnets deposited on miscut Al2O3 substrates. *Appl. Phys. Lett.* **122**, 262404 (2023).
14. Wang, Z. et al. Field-free spin-orbit torque switching of a synthetic antiferromagnet through interlayer Dzyaloshinskii-Moriya interactions. *Cell Rep. Phys. Sci.* **4**, 101334 (2023).
15. Shen, B. et al. Field-free magnetic switching dependence on lateral interfaces in synthetic antiferromagnets by ion implantation. *Appl. Phys. Lett.* **124**, 012401 (2024).
16. Kammerbauer, F. et al. Controlling the interlayer dzyaloshinskii–moriya interaction by electrical currents. *Nano Lett* **23**, 7070–7075 (2023).
17. Wu, C. et al. Field-free spin-orbit torque induced magnetization switching in synthetic antiferromagnet with perpendicular magnetic anisotropy. Preprint at *arXiv* https://doi.org/10.2139/ssrn.4408694 (2023).
18. He, W. et al. Field-free spin–orbit torque switching enabled by the interlayer Dzyaloshinskii–Moriya interaction. *Nano Lett.* **22**, 6857–6865 (2022).
19. Zhao, X. et al. Field-free switching of a spin-orbit-torque device through interlayer-coupling-induced domain walls. *Phys. Rev. Appl.* **13**, 044074 (2020).
20. Fan, H. et al. Field-free spin-orbit torque switching in synthetic ferro and antiferromagents with exchange field gradient. *Adv. Funct. Mater.* **33**, 2211953 (2023).
21. Wei, J. et al. Field-free spin–orbit torque switching in perpendicularly magnetized synthetic antiferromagnets. *Adv. Funct. Mater.* **32**, 2109455 (2022).
22. Kim, H. et al. Field-free switching of magnetization by tilting the perpendicular magnetic anisotropy of Gd/Co multilayers. *Adv. Funct. Mater.* **32**, 2112561 (2022).
23. He, X. et al. Ion-irradiation-induced field-free magnetization switching in synthetic antiferromagnets by spin–orbit torque. *J. Magn. Magn. Mater.* **582**, 170977 (2023).
24. Gupta, R. et al. Harnessing orbital Hall effect in spin-orbit torque MRAM. *Nat. Commun.* **16**, 130 (2025).
25. Go, D. & Lee, H.-W. Orbital torque: torque generation by orbital current injection. *Phys. Rev. Res.* **2**, 013177 (2020).
26. Go, D., Jo, D., Kim, C. & Lee, H.-W. Intrinsic spin and orbital Hall effects from orbital texture. *Phys. Rev. Lett.* **121**, 086602 (2018).
27. Tanaka, T. et al. Intrinsic spin Hall effect and orbital Hall effect in *4d* and *5d* transition metals. *Phys. Rev. B* **77**, 165117 (2008).
28. Go, D., Jo, D., Lee, H.-W., Kläui, M. & Mokrousov, Y. Orbitronics: orbital currents in solids. *EPL Europhys. Lett.* **135**, 37001 (2021).
29. Salemi, L. & Oppeneer, P. M. First-principles theory of intrinsic spin and orbital Hall and Nernst effects in metallic monoatomic crystals. *Phys. Rev. Mater.* **6**, 095001 (2022).
30. Yang, Y. et al. Orbital torque switching in perpendicularly magnetized materials. *Nat. Commun.* **15**, 1–9 (2024).
31. Lee, D. et al. Orbital torque in magnetic bilayers. *Nat. Commun.* **12**, 1–8 (2021).
32. Canonico, L. M., Cysne, T. P., Molina-Sanchez, A., Muniz, R. B. & Rappoport, T. G. Orbital Hall insulating phase in transition metal dichalcogenide monolayers. *Phys. Rev. B* **101**, 161409 (2020).
33. Kim, J. et al. Nontrivial torque generation by orbital angular momentum injection in ferromagnetic-metal/Cu/Al_2O_3 trilayers. *Phys. Rev. B* **103**, L020407 (2021).
34. Bhowal, S. & Satpathy, S. Intrinsic orbital moment and prediction of a large orbital Hall effect in two-dimensional transition metal dichalcogenides. *Phys. Rev. B* **101**, 121112 (2020).
35. Bose, A. et al. Detection of long-range orbital-Hall torques. *Phys. Rev. B* **107**, 134423 (2023).
36. Kontani, H., Tanaka, T., Hirashima, D. S., Yamada, K. & Inoue, J. Giant orbital hall effect in transition metals: origin of large spin and anomalous Hall effects. *Phys. Rev. Lett.* **102**, 016601 (2009).
37. Sala, G. & Gambardella, P. Giant orbital Hall effect and orbital-to-spin conversion in *3d*, *5d*, and *4f* metallic heterostructures. *Phys. Rev. Res.* **4**, 033037 (2022).
38. Go, D. et al. Orbital Rashba effect in a surface-oxidized Cu film. *Phys. Rev. B* **103**, L121113 (2021).
39. Dohi, T. et al. Observation of a non-reciprocal skyrmion Hall effect of hybrid chiral skyrmion tubes in synthetic antiferromagnetic multilayers. *Nat. Commun.* **16**, 8285 (2025).
40. Wang, J. P., Shan, Z. S., Piramanayagam, S. N. & Chong, T. C. Antiferromagnetic coupling effects on energy barrier and reversal properties of recording media. *IEEE Trans. Magn.* **37**, 1445–1448 (2001).
41. Piramanayagam, S. N., Aung, K. O., Deng, S. & Sbiaa, R. Antiferromagnetically coupled patterned media. *J. Appl. Phys.* **105**, 07C118 (2009).
42. Sbiaa, R., Piramanayagam, S. N. & Law, R. Magnetization reorientation in antiferromagnetically coupled Co films and (Co/Pd) multilayers. *Appl. Phys. Lett.* **95**, 242502 (2009).
43. Ranjbar, M., Sbiaa, R., Dumas, R. K., Åkerman, J. & Piramanayagam, S. N. Spin reorientation via antiferromagnetic coupling. *J. Appl. Phys.* **115**, 17C103 (2014).
44. Das, S., Bhatti, S., Maddu, R., Jamshed, B. & Piramanayagam, S. N. Giant damping-like torque efficiency via synergistic spin Hall and enhanced orbital Hall effects. *ACS Appl. Mater. Interfaces* **18**, 3151–3159 (2025).
45. Han, D.-S. et al. Long-range chiral exchange interaction in synthetic antiferromagnets. *Nat. Mater.* **18**, 703–708 (2019).
46. Sbiaa, R. et al. Effect of magnetostatic energy on domain structure and magnetization reversal in (Co/Pd) multilayers. *J. Appl. Phys.* **107**, 103901 (2010).
47. Piramanayagam, S. N. & Zhao, H. B. Effect of seed layers on the textured growth of Pd/Ru intermediate layers for perpendicular recording media. *J. Magn. Magn. Mater.* **312**, 476–479 (2007).
48. Bhatti, S., Das, S., Sekh, B. & Piramanayagam, S. N. CoIr/Pt multilayers enabling physical unclonable function via domain wall motion. *ACS Nano* **19**, 37525–37533 (2025).
49. Bhatti, S. et al. Enhancing damping-like efficiency by low-energy mixed ions bombardment. *Appl. Phys. Lett.* **124**, 022407 (2024).
50. Pai, C.-F., Mann, M., Tan, A. J. & Beach, G. S. D. Determination of spin torque efficiencies in heterostructures with perpendicular magnetic anisotropy. *Phys. Rev. B* **93**, 144409 (2016).
51. Das, S., Bhatti, S. & Piramanayagam, S. N. Boosting charge-to-spin current conversion using orbital Hall effect of Ru with opposing spin-orbit correlated interlayers. *Appl. Phys. Lett.* **127**, 162402 (2025).
52. Lee, S. et al. Efficient conversion of orbital Hall current to spin current for spin-orbit torque switching. *Commun. Phys.* **4**, 234 (2021).

Acknowledgements
The authors gratefully acknowledge the National Research Foundation (NRF), Singapore, for NRF-CRP (NRF-CRP21-2018-0003); the Ministry of Education, Singapore, for its Tier 2 grant MOET2EP50122-0023; and the AcRF Tier 1 grant RG83/2. B.J. and S.D. thank NTU for providing a research scholarship at the University. S.N.P. discloses support for the research of this work from the National Research Foundation, Singapore [NRF-CRP21-2018-0003], Ministry of Education, Singapore [MOE-T2EP50122-0023 and AcRF Tier 1 grant RG83/2]. Open Access funding enabled and organised by the NTU startup grant of S.N.P. M.K. acknowledges support from the German Research Foundation (DFG, projects #268565370 CRC TRR173 Spin+X A01, B02, A12) and from the European Horizon Europe Framework Programme under an EC Grant Agreement N°101129641 "OBELIX". We thank TopDyn - Dynamics and Topology for supporting the collaboration, student and staff exchange between NTU and JGU Mainz.

Author contributions
B.J. and S.D. contributed equally to this work by conducting experiments, analysing and interpreting data, and writing the paper. W.L.W. performed VSM measurements. P.K.M performed the micromagnetic simulations. M.K. supported the study and suggested experiments. S.N.P. conceptualised led and designed the study, provided guidance throughout the research process and conducted thorough reviews during the writing process. All the authors contributed to reviewing the manuscript.

Competing interests
The authors declare no competing interests.

Additional information
Supplementary information The online version contains supplementary material available at https://doi.org/10.1038/s41467-026-72894-8.

Correspondence and requests for materials should be addressed to S. N. Piramanayagam.

Peer review information *Nature Communications* thanks the anonymous reviewer(s) for their contribution to the peer review of this work. A peer review file is available.